Chemical Science

ROYAL SOCIETY OF CHEMISTRY

EDGE ARTICLE

View Article Online
View Journal | View Issue

Cite this: *Chem. Sci.*, 2024, **15**, 6385

All publication charges for this article have been paid for by the Royal Society of Chemistry

Received 19th December 2023
Accepted 9th February 2024

DOI: 10.1039/d3sc06805f

rsc.li/chemical-science

Electrocatalytic CO_2 reduction to formate by a cobalt phosphino–thiolate complex†

Jeremy A. Intrator, David A. Velazquez, Sicheng Fan, Ellie Mastrobattista, Christine Yu and Smaranda C. Marinescu *

Electrochemical conversion of CO_2 to value-added products serves as an attractive method to store renewable energy as energy-dense fuels. Selectivity in this type of conversion can be limited, often leading to the formation of side products such as H_2. The activity of a cobalt phosphino–thiolate complex ($[Co(triphos)(bdt)]^+$) towards the selective reduction of CO_2 to formate is explored in this report. In the presence of H_2O, selective production of formate (as high as 94%) is observed at overpotentials of 750 mV, displaying negligible current degradation during long-term electrolysis experiments ranging as long as 24 hours. Chemical reduction studies of $[Co(triphos)(bdt)]^+$ indicates deligation of the apical phosphine moiety is likely before catalysis. Computational and experimental results suggest a metal-hydride pathway, indicating an ECEC based mechanism.

Introduction

Due to the inherent unsustainable nature of fossil fuels, the development of renewable energy alternatives, which can sustain the rising global energy demands without detrimental environmental impacts, is paramount.[1,2] Unfortunately, large scale application of these sources such as solar and wind, has been deficient due to their intermittent nature, with peak supply often asynchronous with matching demand.[3] To combat this issue, the storage of renewable energy into chemical bonds during peak supply has been proposed to mitigate this spatio-temporal demand mismatch.[4–9] In one strategy, naturally abundant small molecules, such as H_2O and CO_2, are electrochemically converted into value added products, such as H_2 in the hydrogen evolution reaction (HER) and C_1 products in the CO_2 reduction reaction (CO_2RR).[7,10–15] One possible route towards small molecule-based energy storage is the reduction of CO_2 to formate/formic acid (Scheme 1, eqn (1)), due to its unique opportunities towards energy storage and conversion. While other CO_2RR products potentially need additional chemical steps to yield substrates amenable to energy extraction, such as in the case of CO, formate/formic acid can be directly and effectively employed in fuel cells.[16,17] Additionally, formic acid can be effectively utilized as a easily transportable and non-toxic "liquid H_2 carrier", which can release H_2 *via* oxidation back to CO_2.[17–19] One strategy of reducing CO_2 to formate is through hydrogenation with gaseous H_2 (Scheme 1, eqn (2)).[11,20] Drawbacks of this approach are the necessary high pressure and temperatures needed to drive these reactions.[11,20] As a result, decoupling the addition of protons and electrons through electrochemical methods has been a proposed solution to circumvent this issuse (Scheme 1, eqn (1)).

Amongst homogeneous elesctrocatalysts active in the CO_2RR, production of formate is rare,[7,20,21] with selective formate producing electrocatalysts based on earth-abundant elements with FE > 85% even more scarce due to the competitive HER.[17,22] Some electrocatalysts of note that are highly selective towards formate production include iridium pincer complexes that display faradaic efficiency (FE) of 85–97%.[23–25] Platinum phosphine complexes were also reported to electrocatalyze the reversible conversion between CO_2 and HCO_2^- with high selectivity and a low overpotential of 90 mV.[26–29] Dinuclear rhodium complexes were also reported as active electrocatalysts for CO_2 reduction to formate with FEs up to 93%.[30] Catalysts based on non-precious elements, such as the Fe-carbonyl clusters containing an interstitial N atom have been reported to perform the CO_2RR selectively with FE as high as 96% in aqueous media.[31] Notably, upon exchanging the nitrogen atom for carbon in the Fe-carbonyl clusters, the selectively shifts toward the HER, indicating the hydricity of the cluster can be tuned and it drastically affects reactivity.[32] A similarly selective cobalt–pentadienyl complex incorporating a disphosphine ligand amended with two pendant amines was reported to selectively produce formate with 90% FE and at high turnover frequency (TOF > 1000 s^{-1}).[33] Moreover, ligand functionalization has also been reported to alter CO_2RR product selectivity, as in the case of a series of manganese carbonyl bipyridine and phenanthroline complexes where functionalization of the ligand framework with tertiary amines

Department of Chemistry, University of Southern California, Los Angeles, CA, 900089, USA. E-mail: smarines@usc.edu

† Electronic supplementary information (ESI) available. CCDC 2215209. For ESI and crystallographic data in CIF or other electronic format see DOI: https://doi.org/10.1039/d3sc06805f

within the secondary coordination sphere shifted selectivity from CO_2-to-CO towards CO_2-to-formate production, with selectivity towards HCO_2^- reported as large as 89% FE.[34] Recently, the combination of the CO_2 electrocatalyst, $[Mn^I(bpy)(CO)_3Br]$ (bpy = 2,2′-bipyridine), with a concerted proton-electron transfer (CPET) mediator, a synthetic iron-sulfur cluster, was reported to reverse the product selectivity from CO to formate through the formation of a manganese hydride intermediate at an overpotential of 22–340 mV.[35] Lastly, an iron tetradentate phosphine complex was reported to display exceptionally high formate selectivity as large as 97% FE, and was shown to form methanol in the presence of an amine cocatalyst.[36] Though these previous reported catalysts provide a useful knowledge in understanding CO_2RR formate selectivity, the scarcity of these reports in the literature necessitates additional research into new catalytic platforms that can provide additional knowledge in controlling the selectivity of these systems in the CO_2RR.

While the current state of artificial CO_2RR and HER catalysts is limited, evolution has provided highly efficient catalytic systems for these reactions in biological settings. Enzymes such as hydrogenase can reversibly catalyze the HER and the hydrogen oxidation reaction, while CO dehydrogenase and formate dehydrogenase can selectively and reversibly convert CO_2 to CO or formate, respectively, near the thermodynamic potential.[11,37–39] While some research has explored the reactivity of these enzymes directly as electroactive catalysts,[40–42] synthetic chemists have studied metal complexes with common structural motifs located in the active sites of these enzymes for insights into their catalytic performance. One such common motif is the extensive presence of thiolate moieties, which have been subsequently incorporated into reported catalysts for both the HER and CO_2RR.[7,21] Cobalt pyridyl thiolates incorporating diphosphine ancillary ligands have exemplified significant activity and selectivity towards electrocatalytic CO production with FE >92%, and low overpotentials (180 mV) accessible due to the proton shuttling of the activating ligand.[43,44] A similar pyridyl cobalt thiolate complex incorporating bipyridine ligands displays markedly low overpotentials (as low as 110 mV), modest TOFs, selectivity towards formate production as high as 64%, but suffers from catalyst deactivation due to CO poisoning.[45] A cobalt complex incorporating the non-innocent phosphinobenzenethiolate ligand has been reported to produce variable $CO:H_2$ ratios as a function of acid pK_a with faradaic efficiencies >99%.[46] A structurally-derived formate dehydrogenase-based catalyst has also been synthesized, comprising of a Ni bis(dithiolene) metal center with the dithiolene ligands structurally similar to the molybdopterin motif found in the active center of the enzyme.[47,48] This catalysts was notably selective towards

(1) $CO_2 + 2e^- + 2H^+ \rightleftharpoons HCOOH$

(2) $CO_2 + H_2 \rightleftharpoons HCOOH$

Scheme 1 Uses of formate/formic acid towards energy storage and conversion.

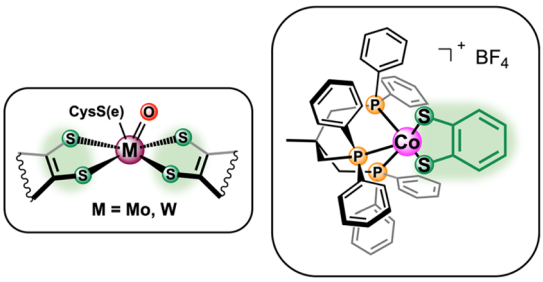

Fig. 1 Chemdraw illustration of the active site of formate dehydrogenase (left) and of a synthetic cobalt triphosphine–thiolate complex ([Co(triphos)(bdt)]$^+$) (right) studied here, depicting the dithiolene motif.

formate production, though a prior irreversible reduction of the ligand is necessary to produce the active catalyst.[47,48] Similarly, a biologically inspired bimetallic oxo Mo–Cu benzenedithiolate complex derived from the active site of Mo–Cu CO dehydrogenase was reported to display formate selectivity of 74%, with experimental data indicating that oxo transfer to CO_2 to form carbonate is necessary before the active catalyst could be generated.[49] Though these prior studies have demonstrated positive results of the use of metal complexes with metal-thiolate motif towards small molecule reduction, there still exists a scarcity of catalytic reports on sulfur-based metal complexes towards these catalytic processes, necessitating the continual study in this area.

Motivated by the success of aforementioned cobalt-based thiolate complexes towards the electrocatalytic reduction of small molecules, herein we report the reactivity of a biologically inspired cobalt based catalyst ([**Co(triphos)(bdt)**]$^+$) incorporating 1,1,1,-tris(diphenylphosphinomethyl) ethane (triphos) and 1,2-benezenedithiolate as the ancillary ligands towards the electrocatalytic CO_2RR (Fig. 1). A multidentate phosphine donor ligand was chosen as an ancillary ligand due to its extensive use in catalysts active towards the chemical[11,50] and electrochemical[7,21,22,50] CO_2RR. Moreover, triphos was selected as the phosphine ligand of choice based on reports of Co-triphos complexes active towards the HER[51] and towards the CO_2 hydrogenation to methanol,[52] in addition to a similarly constructed **Fe(triphos)(bdt)** complex reported as an active HER electrocatalyst.[53] Cyclic voltametric studies were performed to characterize the electrochemical behavior of **[Co(triphos)(bdt)]**$^+$ under reducing conditions, and the reactivity of the complex in the presence of CO_2 and Brønsted acids was investigated. Controlled potential electrolysis studies were employed to explore the selectivity of the catalyst under various conditions and the reaction intermediates were synthesized and characterized *via* NMR spectroscopy to determine possible mechanistic pathways. Lastly, density functional theory (DFT) computational methods were utilized to help elucidate potential mechanistic pathways.

Results and discussion

Complex **[Co(triphos)(bdt)]**$^+$ was synthesized according to a reported literature procedure.[54,55] Cyclic voltammograms (CVs) of

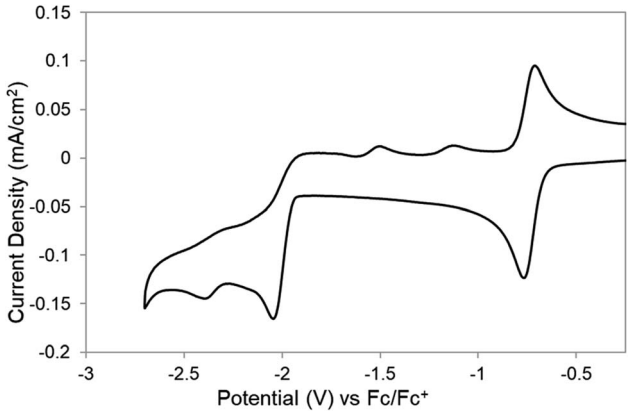

Fig. 2 CVs of 0.5 mM of **[Co(triphos)(bdt)]**$^{+}$ in a CH_3CN solution containing 0.1 M [nBu$_4$N][PF$_6$] under an atmosphere of N_2. Scan rate is 100 mV s^{-1}.

[Co(triphos)(bdt)]$^{+}$ (0.5 mM) were obtained under an N_2 atmosphere using a glassy carbon electrode (GCE) in acetonitrile (CH_3CN) solutions with 0.1 M tetrabutylammonium hexafluorophosphate ([nBu$_4$N][PF$_6$]) as the supporting electrolyte. All potentials are referenced *versus* Fc$^{0/+}$ and all CVs were first scanned cathodically and subsequently returned anodically. All experiments were started at 0 V *vs.* Ag/Ag^{+} of the pseudoreference Ag electrode unless otherwise stated. CVs of **[Co(triphos)(bdt)]**$^{+}$ reveal a reversible redox couple (ΔE_p of 61 mV) at −0.74 V (Fig. 2). This reversible feature is attributed to a formal Co$^{III/II}$ process based on previous reports and is assigned to the **[Co(triphos)(bdt)]**$^{+/0}$ couple.[54–56] The potential at which the Co$^{III/II}$ process occurs is similar to the one observed for other cobalt-based complexes of similar ligand design.[33,44,45] Upon scanning further cathodically, CVs exhibit an irreversible feature at −2.08 V, and an quasi-reversible couple at −2.39 V (ΔE_p of 77 mV), and these features are assigned to the **[Co(triphos)(bdt)]**$^{0/-}$ and **[Co(triphos)(bdt)]**$^{-/-2}$ couples, respectively (Fig. 2). Scanning anodically from this potential, two irreversible redox events are observed at −1.51 V and −1.13 V. These oxidation features do not appear in the CVs if the potential is reversed before reaching **[Co(triphos)(bdt)]**$^{0/-}$, suggesting that these oxidative events originate from the reduction of **[Co(triphos)(bdt)]**^{0} (Fig. S1†). The irreversible nature of the redox feature of the **[Co(triphos)(bdt)]**$^{0/-}$ is likely due to a chemical/structural change to the complex in conjunction with the associated reduction of the complex (*vide infra*). CVs of variable scan rates performed on the **[Co(triphos)(bdt)]**$^{0/-}$ feature (Fig. S2–S4†) do not display any change in the reversibility of the feature, though some changes were observed in the return oxidation features. This may be a result of the chemical step occurring too rapid to be observed compared to the CV timescale. Due to the irreversibility of the **[Co(triphos)(bdt)]**$^{0/-}$ couple, Randles–Sevcik analysis was not employed and therefore the diffusivity of the species could not be determined.

To understand the electrochemical behavior observed at the **[Co(triphos)(bdt)]**$^{0/-}$ couple, **[Co(triphos)(bdt)]**^{0}, which has one unpaired electron (Fig. S5†), was chemically reduced using excess KC_8 and in the presence of 18-crown-6 (Scheme 2). X-ray quality crystals were grown *via* vapor diffusion of *n*-pentane into tetrahydrofuran solutions containing the reduced complex. Solid state structure of this species indicates a four-coordinate cobalt complex with the triphos ligand acting as a bidentate ligand in this structure, with one of the phosphine linkers dissociated from the metal center (Fig. 3). The angular structural parameter, τ, was calculated to be ∼0.3 (eqn (S1)†), suggesting that the metal center adopts a distorted square planar geometry, with a torsion angle of 30.91°. Additionally, a single potassium cation chelated by 18-crown-6 is present as a counterion for each molecular unit in the lattice, suggesting this complex can be identified as **[Co(triphos)(bdt)][K(18-crown-6)]**.

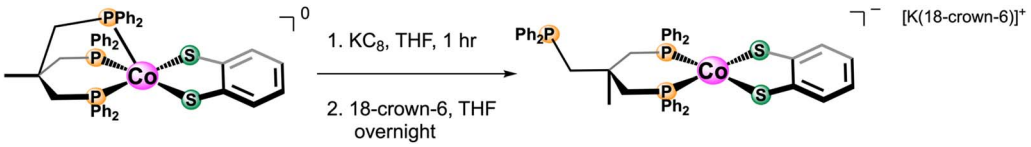

Scheme 2 Synthetic procedure for the reduction of **[Co(triphos)(bdt)]**^{0} to **[Co(triphos)(bdt)][K(18-crown-6)]**.

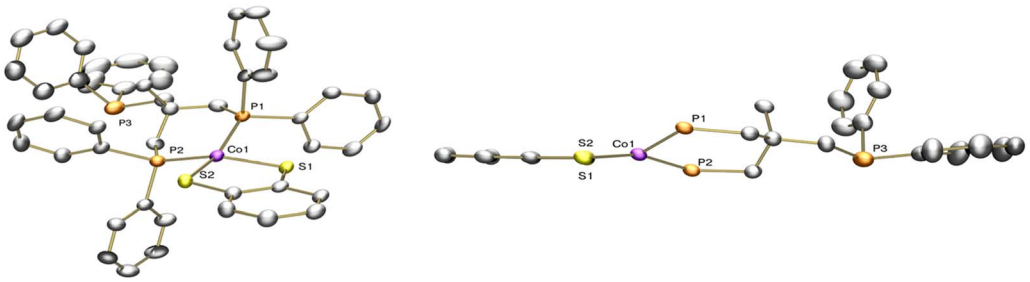

Fig. 3 Solid-state structure of **[Co(triphos)(bdt)][K(18-crown-6)]**. Aryl and aliphatic protons, counterions, and solvent molecules are omitted for clarity.

Table 1 Average selected bond lengths (Å) for [Co(triphos)(bdt)]^x complexes, where $x = 1, 0, -1$

	Bond length (Å)		
Bond	[Co(triphos)(bdt)]$^+$	[Co(triphos)(bdt)]^0	[Co(triphos)(bdt)]$^-$
Co–S	2.169(2)	2.223(1)	2.186(1)
Co–P_{apical}	2.183(2)	2.300(1)	—
Co–P_{basal}	2.232(2)	2.212(1)	2.107(1)
C–S	1.734(4)	1.750(4)	1.750(3)
Reference	55	57	This work

Average bond lengths for **[Co(triphos)(bdt)]$^-$** can be found in Table 1 in addition to those reported for **[Co(triphos)(bdt)]$^+$** and **[Co(triphos)(bdt)]^0**.[55,57] Although an elongation of the Co–S bond from 2.169(2) to 2.223(1) Å is reported upon reduction of **[Co(triphos)(bdt)]$^+$** to **[Co(triphos)(bdt)]^0**, a subsequent contraction of the Co–S bond to 2.186(1) Å is observed upon further reduction to **[Co(triphos)(bdt)]$^-$**. On the other hand, consecutive contractions of the basal Co–P bond (labeled as Co–P_{basal}) are observed from 2.232(2) Å in **[Co(triphos)(bdt)]$^+$** to 2.212(1) Å in **[Co(triphos)(bdt)]^0**, and then to 2.107(1) Å in **[Co(triphos)(bdt)]$^-$**. Additionally, while the C–S bond length was observed to slightly elongate from 1.734(4) to 1.750(4) Å upon reduction from **[Co(triphos)(bdt)]$^+$** to **[Co(triphos)(bdt)]^0**, no change to the bond length is observed upon generating **[Co(triphos)(bdt)]$^-$** (C–S bond of 1.750(3) Å in **[Co(triphos)(bdt)]$^-$**), indicating the innocent nature of the dithiolene ligand at the **[Co(triphos)(bdt)]$^{0/-}$** couple.

To determine if the solution-state structure of **[Co(triphos)(bdt)]$^-$** is comparable to that of its solid-state structure, ^{1}H and ^{31}P-{^{1}H} nuclear magnetic resonance (NMR) spectrum of **[Co(triphos)(bdt)][K(18-crown-6)]** were acquired at varying temperatures (Fig. 4 and S6–S12†). At 26 °C, the ^{31}P-{^{1}H} NMR spectrum of **[Co(triphos)(bdt)][K(18-crown-6)]** in acetonitrile-d_3 displays two broad peaks at δ 46.7 and −31.0 ppm (Fig. 4a). At −35 °C (Fig. 4a and S12†), two sharp peaks are observed at δ 41.8 and −28.2 ppm in a 2 : 1 ratio and are attributed to both the bound and un-bound phosphines, respectively. The ^{1}H NMR spectrum of **[Co(triphos)(bdt)][K(18-crown-6)]** in acetonitrile-d_3 at 26 °C (Fig. 4b, c and S6–S8†) displays two broad aliphatic singlets at δ 2.23 (s) and 0.41 (s) ppm in a 6 : 3 ratio corresponding to the methylene and methyl moieties on the triphos ligand, respectively. Three aromatic signals appear at δ 6.43 (m), 7.21 (m), and 7.24 (m) ppm attributed to the aromatic protons on both the dithiolene and triphos ligand, in addition to a broad peak at δ 7.75 pm. At −35 °C, the ^{1}H NMR spectrum of **[Co(triphos)(bdt)][K(18-crown-6)]** in acetonitrile-d_3 (Fig. 4b, c, S6–S8 and S10†) displays three new features in the aliphatic region, including two doublets at δ 2.26 and 2.19 ppm and a singlet at δ 2.04 ppm in a ratio of 2 : 2 : 2 attributed to the individual methylene linkers on both the ligated phosphine and the unbound phosphines, respectively, and three new aromatic singlets at δ 8.10, 7.68, and 7.26 ppm, attributed to the aromatic protons of the unbound phosphine of the triphos ligand. The reversibility of the observed temperature-dependent solution-state changes was investigated by remeasuring the ^{1}H and ^{31}P NMR spectra of **[Co(triphos)(bdt)][K(18-crown-6)]** at room temperature (Fig. S9 and S11†), and the observed spectra are identical to the ones observed previously. The presence of peak coalescence and broadening in the proton and phosphorus resonances of **[Co(triphos)(bdt)][K(18-crown-6)]** at room temperatures is indicative of a fast exchange process on the NMR timescale. As the temperature is decreased the exchange can be limited. The ^{31}P NMR spectrum at −35 °C is indicative of two different phosphine environments in the 2 : 1 ratio, corresponding to the bound and deligated phosphines, respectively. The ^{1}H NMR spectrum of **[Co(triphos)(bdt)]$^-$** at low temperatures also suggests that one of the phosphine in the triphos ligand is dissociated from the metal center. These results indicate that the low temperature solution-state structure is in agreement with the solid-state crystal structure. The ^{1}H and ^{31}P-{^{1}H} NMR spectra of **[Co(triphos)(bdt)][K(18-crown-6)]** at room temperature suggest that the deligated phosphine is interchanging with the bound phosphine moieties in a fast exchange process. Based on the variable temperature (VT) NMR data obtained of the bound methylene linkers in **[Co(triphos)(bdt)][K(18-crown-6)]**, the exchange rate constant (k_c) and the free energy of activation ($\Delta G^{\ddagger}$) at coalescence were determined to be 129 s^{-1} and 13.5(0.5) kcal mol^{-1}, respectively (eqn (S2) and (S3)†). Consequently, VT studies indicate similar low temperature solution state and solid-state crystal structures where one phosphine moiety is deligated from the metal center, whereas at room temperature a fast exchange is observed. This

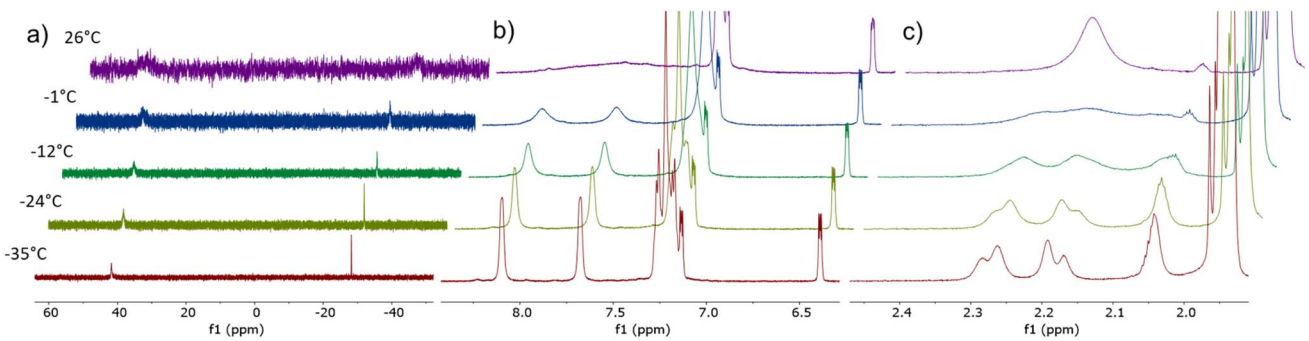

Fig. 4 Variable temperature overlay of: (a) 600 MHz ^{31}P-{^{1}H} NMR spectra of **[Co(triphos)(bdt)][K(18-crown-6)]** in acetonitrile-d_3; 600 MHz ^{1}H NMR spectra of **[Co(triphos)(bdt)]$^-$** in (b) aromatic and (c) aliphatic region in acetonitrile-d_3. Temperature varied between 26 and −35 °C.

chemical step is likely the origin of the irreversibility of the **[Co(triphos)(bdt)]$^{0/-}$** couple.

The electrochemistry of the isolated **[Co(triphos)(bdt)]-[K(18-crown-6)]** complex was explored under N_2 and displays similar redox features as the ones observed in the CVs of **[Co(triphos)(bdt)]$^+$** (Fig. S13†), indicating the isolated species is identical to that generated at the **[Co(triphos)(bdt)]$^{0/-}$** couple. A slightly lower current density for the **[Co(triphos)(bdt)]$^{0/-}$** couple is observed on the first scan. The catalytic behavior of **[Co(triphos)(bdt)]$^+$** was studied using CV experiments in the presence of CO_2 and with variable proton sources. CVs of **[Co(triphos)(bdt)]$^+$** under CO_2 display enhanced current densities at potential corresponding to the irreversible **[Co(triphos)(bdt)]$^{0/-}$** couple (Fig. 5). An anodic shift is observed at the onset of the **[Co(triphos)(bdt)]$^{0/-}$** couple under CO_2, indicative of an association of CO_2 to the metal center upon reduction, suggesting an EC mechanism.[58–60] Upon scanning anodically, the oxidative features at −1.51 V and −1.13 V are not observed under CO_2, suggesting a new faradaic process occurs in the presence of CO_2 that consumes the electrons that would otherwise be available for oxidation at these features. Addition of 0.3 M of a Brønsted acid, such as 2,2,2-trifluoroethanol (TFE), under a CO_2 atmosphere leads to the formation of a characteristic catalytic plateau, with a 5-fold increase in the current density (Fig. 5). Increasing the concentration of TFE yields an increase in the catalytic current density and an anodic shift in the catalytic onset potential (Fig. S14†). Upon reaching 0.7 M TFE, a new feature appears at −2.54 V, which progressively increases in current density upon further titration of TFE (Fig. S14†) and could be attributed to background activity from the glassy carbon electrode (Fig. S15†). Addition of 0.3 M TFE under N_2 display a moderate increase in the current response at the **[Co(triphos)(bdt)]$^{0/-}$** couple (Fig. S16 and S17†), which represents a 2.5-fold decrease in the current density displayed under CO_2. CVs studies performed in the absence of catalyst indicate a different shape of the trace, such as a peak-like feature, and large current densities from the bare glassy carbon electrode (Fig. S18 and S19†).

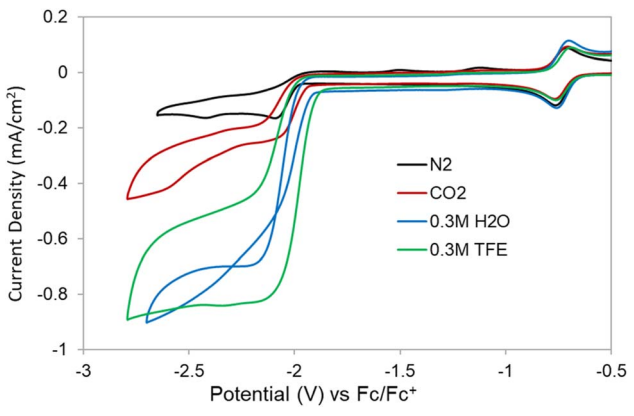

Fig. 5 CVs of 0.5 mM of **[Co(triphos)(bdt)]$^+$** in a CH_3CN solution containing 0.1 M [nBu$_4$N][PF$_6$] under an atmosphere of N_2 (black), CO_2 (red), and under CO_2 in the presence of 0.3 M H_2O (blue) or 0.3 M TFE (green). Scan rate is 100 mV.

Addition of 0.3 M H_2O as a proton source under a CO_2 atmosphere yields a catalytic response that displays a trace-crossing event upon scanning anodically (Fig. 5). This phenomenon has been previously attributed to the formation and subsequent reduction of a newly formed species with a standard reduction potential more positive than that of **[Co(triphos)(bdt)]$^{0/-}$**.[61–63] Notably, this trace-crossing event is not observed in the CVs performed with scan rates of 0.5 and 1 V s^{-1} (Fig. S20†), suggesting that at fast scan rates the rate of formation of this species is too sluggish to be observed on the CV timescale.[34] Titrations of H_2O beyond the 0.3 M concentration yields CV traces that decrease in catalytic current, which is in contrary to what is expected for CO_2RR dependent on proton concentration (Fig. S21†), indicating a separate chemical step is occurring in conjunction with the CO_2RR or may be a result of a loss of catalyst solubility at large [H_2O]. Titration of H_2O at lower concentrations (40–100 μM) yield CV traces that increase in current, suggesting this additional chemical step is disfavored at low acid concentrations (Fig. S22†). Addition of D_2O was performed under a CO_2 atmosphere at similarly low concentrations, giving rise to a H/D kinetic isotope effect (KIE) of 5.9(8) (Fig. S23†). This large value indicates that protons are involved in the rate determining step, and based on prior literature studies a hydride-based mechanism may be possible, either through protonation of the metal center or transfer to CO_2.[33,45] Further addition of both H_2O or D_2O past 0.1 M leads to no subsequent increase in current, indicative of saturation kinetics. Addition of 0.3 M H_2O under N_2 displays only a minor increase in current at the **[Co(triphos)(bdt)]$^{0/-}$** couple (Fig. S24†). The onset of the **[Co(triphos)(bdt)]$^{0/-}$** couple shifts anodically as [H_2O] increases, indicating association of a substrate upon initial reduction (EC mechanism), which in this case suggests the formation of a metal-hydride. Additionally, the oxidative features at −1.51 V and −1.13 V are still present at all [H_2O] under N_2 (Fig. S25†), suggesting that the current response is not catalytic and no faradaic process is present to consume the electrons provided at the **[Co(triphos)(bdt)]$^{0/-}$** couple which can be subsequently oxidized. Moreover, the trace-crossing behavior in not observed in a CV study performed in the absence of **[Co(triphos)(bdt)]$^+$** (Fig. S26†).

To identify and quantify the products generated at the observed catalytic features, controlled potential electrolysis (CPE) experiments were performed in acetonitrile for 2 hours under 1 atm of CO_2 with either TFE or H_2O as the proton source. CPEs were performed with both TFE and H_2O either at −2.15 V or at −2.60 V *vs.* Fc$^{0/+}$ and with various acid concentrations to determine if the product selectivity and total turnover number changes as a function of these variables. At the end of the CPE experiment, gaseous products were sampled from the head space of the electrolysis cell, and quantification was determined by gas chromatography (GC) analysis. Products in the liquid phase were detected and quantified using ^{1}H NMR spectroscopy and ion chromatography. Results of these experiments are shown in Fig. S27, S28 and Table S1† for the analyses using ^{1}H NMR spectroscopy and in Table 2, Fig. 6 and S29,† for analyses using ion chromatography. ^{1}H NMR spectroscopy method does not allow for the detection of oxalate, therefore, quantification

using ion chromatography will be the method discussed in the main text (Table 2), but results from both methods are included in the ESI.† Turnover numbers (TONs) and faradaic efficiencies (FE%) were determined from the CPE studies, based on established equations (see ESI† for details). A total of three runs were performed for each condition studied and the reported FE% and TONs are an average of these values. Electrolysis of **[Co(triphos)(bdt)]$^+$** in the presence of 0.3 M TFE at −2.15 V (entry 1) yields formate as the primary CO_2 reduction product with a faradaic efficiency (FE) of 67%. Oxalate is also detected with a FE of 16%. Gaseous products such as H_2 and CO were detected with FEs of 8% and 1.1%, respectively, yielding a combined FE% of 93%.

Upon employing H_2O as a proton source (entry 2), CPE results display a significant shift in selectivity towards formation of formate at 93%, with FEs of oxalate, H_2, and CO, detected to be 5%, 5%, and 1% respectively, resulting in a near unity total FE% considering all products detected. An initial increase in the absolute value of the catalytic current is observed in the CPEs employing H_2O as a proton source (Fig. S27 and S29†), which is in contrary to the initial decrease in current expected in electrolysis experiments due to the initial rapid consumption of substrate in the electrode's double layer. This preliminary induction period may indicate the formation of a more active form of the **[Co(triphos)(bdt)]$^+$** catalyst, which may also be associated with trace-crossing events observed in the CVs experiments under CO_2 and in the presence of H_2O. After this initial increase in the absolute value of the catalytic current, stable currents are observed throughout the rest of the CPE (Fig. S27 and S29†). Performing CPE at a larger overpotential (−2.60 V) in the presence of 0.3 M H_2O (entry 3) yields a similar selectivity towards formate production (92%), and a higher $HCOO^-$ TONs (12.6) compared to that observed at −2.15 V (4.0). Additionally, a similar product distribution is observed between both operating potentials: 5% oxalate, 8% H_2, and 0.3% CO. Moreover, performing electrolysis with 0.6 M H_2O at −2.15 V (entry 4) results in a similar selectivity for formate production (94%), along with 7% FE for H_2, and trace amounts of CO and oxalate. Performing CPE at −2.15 V without an added exogenous Brønsted acid (Table S1,† entry 5) yields only trace gaseous products and minor amounts of formate detected, with a TON of 0.01 and a FE% of 3%, indicating the presence of a proton donor is necessary for significant product formation. Lastly, performing the CPE at −2.15 V with 0.3 M H_2O under a nitrogen atmosphere displays low current (Fig. S27 and S29†), and yields only trace amounts of gaseous and liquid products. Performing the CPE at −2.15 V with 0.3 M TFE under a nitrogen atmosphere displays a more moderate current (Fig. S29†), and yields H_2 as a major product whereas other products are trace or non-detectable.

Due to high selectivity towards formate production in the presence of 0.3 M H_2O at −2.15 V, additional control, long term stability, and degradation experiments were performed under these conditions. Control experiments in the absence of catalyst yield only trace amounts of CO_2RR products (Fig. S27†), indicating the presence of **[Co(triphos)(bdt)]$^+$** is necessary to generate the products discussed above. Performing CPE experiments for 8 hours displays good current stability and exhibits a notable increase in selectivity towards formation of formate at 91% as indicated by ^{1}H NMR spectroscopy quantification method, with a total formate TON of 24.3 (Fig. S30 and Table S1† entry 6). CVs of the electrolysis solution post-CPE display an increase in current relative to the currents observed in the CVs performed before electrolysis experiments (Fig. S30b†), in agreement with the observed initial increase in the absolute value of the catalytic current displayed in the 8 h CPE traces (Fig. S30a†). To determine if a catalytically active phase is depositing on the electrode during electrolysis, the working electrode was rinsed with clean CH_3CN post-electrolysis and placed back in the working compartment with a CH_3CN solution containing 0.1 M [nBu$_4$N][PF$_6$] and 0.3 M H_2O under an atmosphere of CO_2. CVs of the electrodes post-CPE display negligible current density, with currents comparable to those observed using a bare glassy carbon electrode (Fig. S31†). Performing a 2 h-electrolysis with the rinsed post-CPE electrode produces only trace products as indicated by gas chromatography for the gas phase and ^{1}H NMR spectroscopy quantification method for the liquid phase, suggesting no catalytically active phase is deposited on the electrodes during CPE (Fig. S32†). The rinsed electrode was additionally analyzed using X-ray photoelectron spectroscopy (XPS) to determine if a cobalt-containing species is deposited on the working electrode during electrolysis. XPS spectra of the working electrode indicates trace amounts of cobalt and sulfur on the electrode surface (Fig. S33†). XPS spectra of a GCE immersed in a 0.5 mM CH_3CN solution of **[Co(triphos)(bdt)]$^+$** exhibits similar Co 2p

Table 2 Summary of the controlled potential electrolysis results from Fig. S29 and their analyses *via* gas and ion chromatography for the gas and liquid phase, respectively, along with the conditions used for the electrolysis of [Co(triphos)(bdt)]$^+$ in the presence of CO_2 and a proton source. Electrolyses were performed with 0.5 mM of [Co(triphos)(bdt)]$^+$ in a CH_3CN solution containing 0.1 M [nBu$_4$N][PF$_6$] under an atmosphere of CO_2

						H_2		CO		$HCOO^-$		$C_2O_4^{2-}$		
Entry	Acid	Time (h)	Acid (M)	Potential (V) *vs.* $Fc^{0/+}$	Charge (C)	TON (±0.05)	FE% (±3)	TON (±0.03)	FE% (±2)	TON (±0.03)	FE% (±4)	TON (±0.02)	FE% (±2)	Total FE% (±6)
1	TFE	2	0.3	−2.15	19.9	0.51	8	0.07	1.1	3.9	67	0.9	16	93
2	H_2O		0.3	−2.15	14.9	0.20	5	0.02	1	4.0	93	0.2	5	103
3			0.3	−2.60	47.4	1.03	8	0.05	0.3	12.6	92	0.7	5	104
4			0.6	−2.15	18.0	0.37	7	Trace	Trace	4.9	94	Trace	Trace	101
5		24	0.3	−2.15	262	5.33	8	1.57	2	64.0	94	1.0	1	105

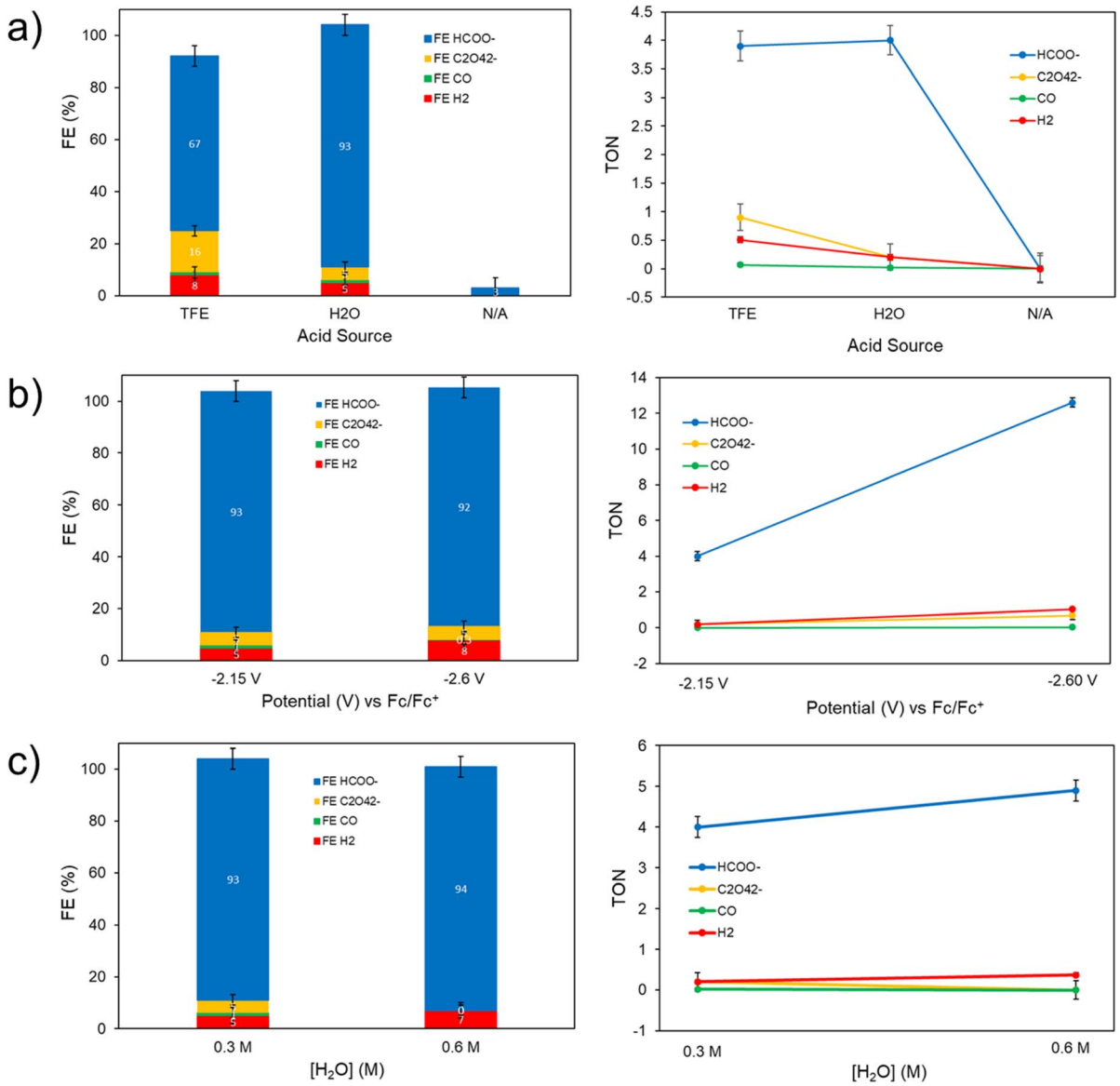

Fig. 6 Comparison of the controlled potential electrolysis results from Fig. S29† – faradaic efficiencies (FE%) and turnover numbers (TONs) quantified *via* gas and ion chromatography for the gas and liquid phase, respectively – in the presence of: (a) 0.3 M TFE, 0.3 M H_2O, or no exogenous proton source (N/A) at −2.15 V *vs.* $Fc^{0/+}$, (b) 0.3 M H_2O at potentials of −2.15 or −2.60 V *vs.* $Fc^{0/+}$, and (c) 0.3 or 0.6 M H_2O at −2.15 V *vs.* $Fc^{0/+}$. All electrolyses were performed with 0.5 mM of **[Co(triphos)(bdt)]**$^+$ in a CH_3CN solution containing 0.1 M $[nBu_4N][PF_6]$ under an atmosphere of CO_2.

and S 2p features with those displayed in the spectra of the post-electrolysis electrode, suggesting that these features originate from physiosorbed material, and that chemical deposition of cobalt-containing materials on the electrode surface during electrolysis is unlikely (Fig. S33†). A similar long-term electrolysis was performed with 0.5 mM **[Co(triphos)(bdt)]**$^+$ in the presence of 0.3 M H_2O and 1 atm of CO_2 at −2.15 V for 24 hours (Fig. S34†), and the products generated were analyzed *via* gas and ion chromatography for the gas and liquid phase, respectively. Formate was detected with a FE of 94% and a TON of 64.0, along with other minor products, such as oxalate (1% FE), H_2 (8%), and CO (2%) (Fig. S34† and Table 2 entry 5). The electrolysis cell and electrode were rinsed with CH_3CN and the electrolysis was ran at −2.15 V in the presence of 0.3 M H_2O and 1 atm of CO_2 which afforded only trace amounts of CO (Fig. S35†). XPS of the rinsed electrode indicates trace amounts of cobalt and sulfur on the electrode surface (Fig. S36†), suggesting that chemical deposition of cobalt-containing materials on the electrode surface during electrolysis is unlikely. A CPE experiment was performed with 0.5 mM **[Co(triphos)(bdt)]**$^+$ in the presence of 0.3 M H_2O and 1 atm of CO_2 at −2.15 V and with Hg pool as the working electrode to further validate the homogenous nature of the catalyst. A stable current was observed during the 2 h electrolysis (Fig. S37†). Quantification of the products *via* gas and ion chromatography for the gas and liquid phase, respectively, indicates a slightly reduced

selectivity towards formate production with a FE of 79%, along with other products including oxalate (11% FE), H_2 (6%), and CO (0.3%) (Tables S3 and S4†). These results are relatively similar with the ones observed using a glassy carbon working electrode (Table 2, entry 2), suggesting that the selectivity of **[Co(triphos)(bdt)]$^+$** catalyst is not drastically affected by changing the working electrode, and supporting the homogeneous behavior of the system.

To evaluate the electrocatalytic activity of **[Co(triphos)(bdt)]$^+$**, the CO_2RR selectivity towards formate and overpotential are compared relative to the values reported for other molecular catalysts. Turnover frequency and the use of Tafel plot are avoided in this discussion due to the inherent coupled chemical steps corresponding to **[Co(triphos)(bdt)]$^+$** upon using H_2O as a proton source, as illustrated by CV and CPE plots, in addition to the lack of an "S" shaped curve marking a purely kinetic regime, which makes these values not representative of the CO_2RR catalytic kinetics. In that light, other factors such as relative overpotential and selectivity towards formate are used to help compare the activity of **[Co(triphos)(bdt)]$^+$** relative to other reported catalysts. The overpotential for the CO_2RR to formate (η) is determined by taking the difference of the standard reduction potential of CO_2/HCOOH relative to the applied overpotential and is considered at the applied CPE potential of −2.15 V *vs.* $Fc^{0/+}$ where high selectivity towards formate production was displayed. The standard reduction potential of CO_2 to HCOOH was determined based on methods developed by Savéant and Artero (see ESI† for details).[33,64] Using this method, an overpotential of 750 mV was determined and is compared with other reported electrocatalysts for electrocatalytic CO_2RR with their associated overpotentials and relative selectivities (Table S6†). Selective electrocatalytic conversion of CO_2 to formate >85% FE are quite rare amongst reported electrocatalysts active in the CO_2RR, making **[Co(triphos)(bdt)]$^+$** an effective electrocatalyst towards selective conversion of CO_2 to formate over other side reactions such as HER. Amongst formate selective catalysts employing earth abundant metals, **[Co(triphos)(bdt)]$^+$** displays comparably high selectivities similar to those reported for other catalytic systems such as fac-Mn(N∧N)(CO)$_3$Br,[34] $Fe_4N(CO)_{12}$,[31] and [Fe(PP$_3$)](BF$_4$)$_2$,[36] though at moderately higher operating overpotential (Table S6†). Interestingly, while **[Co(triphos)(bdt)]$^+$** exhibits significant similarities to [CpCo($P^R_2N^{R'}_2$)I] in[33] both structure, selectivity, and effective overpotential, **[Co(triphos)(bdt)]$^+$** displays longer term electrolytic stability (∼8 and 24 hours) compared to [CpCo($P^R_2N^{R'}_2$)I] (∼1 hour). Additionally, **[Co(triphos)(bdt)]$^+$** exhibits superior formate selectivity compared to that observed for reported catalytic systems featuring metal thiolates moieties, which have not been reported to exceed formate selectivity >74% FE and have not been reported to employ water as the exogenous proton source.

To identify potential reaction intermediates, the reactivity of the chemically reduced complex, **[Co(triphos)(bdt)][K(18-crown-6)]**, with CO_2 was investigated. Exposure of 1 atm of CO_2 to a J. Young NMR tube charged with a solution of **[Co(triphos)(bdt)][K(18-crown-6)]** in acetonitrile-d_3 leads to a change in the ^{1}H NMR spectrum (Fig. S38†), suggesting a reaction between the two-electron reduced species and CO_2 and the formation of the paramagnetic **[Co(triphos)(bdt)]^0**. However, upon addition of TFE, no formate or hydride resonances were detected. To gain further understanding of the electrocatalytically active species in solution, additional studies were performed to electrochemically generate **[Co(triphos)(bdt)]$^-$** and investigate its reactivity with CO_2 and proton donors through ^{1}H NMR spectroscopy. Adapting a procedure from Mougel and coworkers,[35] a 2 mM **[Co(triphos)(bdt)][BF$_4$]** in 0.1 M $TBAPF_6/CH_3CN$ (10 mL) was electrochemically reduced at −2.2 V until 95% of the current has decreased, indicating complete conversion of **[Co(triphos)(bdt)]$^+$** to **[Co(triphos)(bdt)]$^-$**. A 1 mL aliquot was taken from the electrolyte solution, evacuated, and transferred to an NMR tube in 1 mL CD_3CN, upon which 50 μL of 2 M TFE in CD_3CN under N_2 were added to the reaction mixture and analyzed *via* ^{1}H NMR spectroscopy (Fig. S39†). No changes were observed in the ^{1}H NMR spectra besides the additional TFE resonances, although possible H_2 may be present in the omitted range due to overlap with the proton resonances from the electrolyte. A similar procedure was employed with another sample of the electrolysis solution, to which 50 μL of CO_2 sparged 2 M TFE in CD_3CN was added to the J. Young NMR tube (Fig. S39†). No hydride resonances were found; however, formate resonances were detected at δ 8.4 ppm. These results indicate that the electrochemical formation of **[Co(triphos)(bdt)]$^-$** is important for catalytic activity.

Based on experimental data, a proposed mechanism for the electrochemical conversion of CO_2 to $HCOO^-$ utilizing **[Co(triphos)(bdt)]$^+$** can be found in Scheme 3. To supplement experimental results, DFT calculation were employed to help elucidate potential intermediates and pathways that were not accessible *via* experimental methods. As formate was found to be the primary CO_2RR product, mechanistic discussion will be limited to this product. Based on obtained electrochemical data, we only observe enhanced currents in the presence of CO_2 and a proton source at the **[Co(triphos)(bdt)]$^{0/-}$** couple. Additionally, NMR studies indicate production of formate from electrochemically generated **[Co(triphos)(bdt)]$^-$** in the presence of CO_2 and a proton source. All these experiments suggest generation of **[Co(triphos)(bdt)]$^-$** (**III**) is necessary before any catalytic activity is observed. Moreover, based on chemical reduction experiments, we can determine an additional chemical step in the form of apical phosphine deligation occurs concurrently upon reduction of **[Co(triphos)(bdt)]^0** (**II**). Calculation of the HOMO of the **III** yields a molecular orbital that displays significant overlap with the thiolate ligand, indicating the relative importance of the thiolate towards the relative energy of the HOMO and as a result the catalytic activity of **III** (Fig. S40†). CVs of **[Co(triphos)(bdt)]$^+$** display an anodic shift at the **[Co(triphos)(bdt)]$^{0/-}$** couple under an atmosphere of CO_2 and in the presence of a proton source under N_2, indicating the favorable binding of both CO_2 and H^+. As a result, DFT calculations were performed to model both Co–H (**IV-H**) or Co–CO_2 (**IV-CO$_2$**) adducts to study their role in the reduction of CO_2 to formate.

Modelling of **IV-CO$_2$** yields a favored structure with CO_2 bound apically in a position *trans* to the methyl moiety of the triphos ligand within a square pyramidal metal coordination

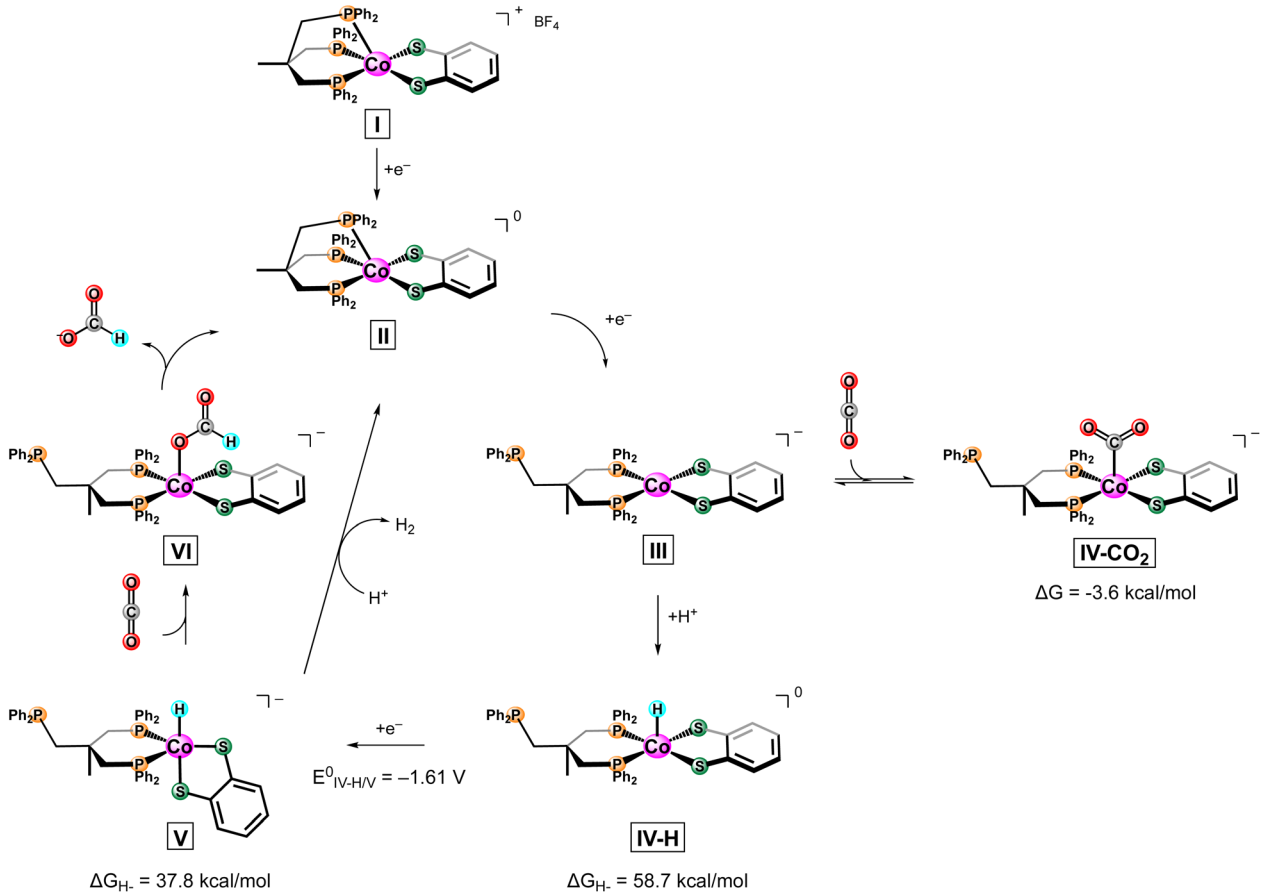

Scheme 3 Proposed mechanism for electrocatalytic CO_2RR to $HCOO^-$ employing **[Co(triphos)(bdt)]$^+$**.

environment favored by 4.8 kcal mol^{-1} compared to its associated isomer (Fig. S41 and S42†). Formation of **IV-CO$_2$** has a free energy change of −3.6 kcal mol^{-1}. This considerably low free energy change can be rationalized due to the large degree of ligand reorientation from that of a distorted square planar structure of **III** to that of a planar geometric orientation in **IV-CO$_2$** upon adduct formation (Fig. S42†). These results, in addition to CO being detected only as a negligible product, indicates that the formation of the CO_2 bound adduct is not the predominant mechanism, and the metal hydride pathway will be considered in this discussion continuing forward.

A large KIE value of 5.9(8) supports a hydride based mechanism, with a rate limiting step (RLS) most likely involving a Co–H formation or transfer step, as reported in related electrocatalysts with similarly large KIE values.[33,45] Modelling of **IV-H** yields a similar result to **IV-CO$_2$**, with the optimized structure displaying a hydride adduct in a position *trans* to the methyl moiety of the triphos ligand, albeit with a smaller relative difference in energy of 1.7 kcal mol^{-1}, indicating that both of these isomers could be present in solution (Fig. S43†). Notably, the calculated structure of **IV-H** retains the distorted square planar structure of both phosphine and thiolate ligands in **II**, with the proton in the apical position (Fig. S44†). Protonation of the dithiolene was also explored due to previous reports of protonation as an initial step before turnover on similarly constructed complexes.[46,65,66] Due to both thiolate moieties being symmetrically inequivalent, four possible thiol permutations were calculated (Fig. S45†). Comparing the calculated **IV-H** structure to the lowest energy Co(S–H) state indicates the metal hydride is the thermodynamically favored product over the thiolate protonation product by 21.4 kcal mol^{-1} (Fig. S46†). As mentioned, this contrasts other similarly reported catalysts that utilize thiolate ligands that display either direct protonation of a sulfur atom on the ligand or protonation of a secondary element of the ligand framework.[43,45,46,49,65,66] Based on these computational results, the thiolate ligand only inductively impacts the active metal center, with significant impact on the energetics of the system as a whole.

Based on the optimized structure of **IV-H** and the calculated energy of a solvated free hydride, the hydricity (ΔG_{H^-}) of **IV-H** was calculated to be 58.7 kcal mol^{-1}. This ΔG_{H^-} value is larger compared to that reported for the hydricity of formate in acetonitrile (44 kcal mol^{-1}) suggesting that a formal hydride transfer from **IV-H** to CO_2 is not thermodynamically favored.[26,67] Similar reports on cobalt hydrides suggest an additional formal reduction of the generated Co(III)–H to Co(II)–H is necessary before a hydride transfer to the substrate can be thermodynamically driven.[33,45,51] As a result, the 1e$^-$ reduction of **IV-H** was

considered and produces complex **V**. The optimized structure of **V** displays a distorted square pyramidal structure ($\tau = 0.62$) with the hydride ligand in the axial position (Fig. S47†). Calculating the hydricity of **V** yields a ΔG_{H^-} of 37.8 kcal mol^{-1}, indicating that reduction of **IV-H** to **V** is necessary to produce a Co–H hydridic enough to convert CO_2 to $HCOO^-$. Moreover, the reduction potential of **IV-H** to **V** was calculated to occur at −1.61 V *vs.* $Fc^{0/+}$ (Table S7†), well anodic of potentials where onset of catalysis is observed, indicating a strong electrochemical driving force for the conversion to **V** upon protonation of **III.** With this in mind, the trace-crossing behavior observed in CVs under catalytic conditions can be rationalized as follows. Protonation of **III** to **IV-H** involves a chemical step. It is possible that **III** diffuses away from the electrode before reacting with proton donors in the bulk solution to form **IV-H**, which is rapidly reduced at the electrode to produce **V**, yielding the observed trace-crossing at low scan rates. The calculated reduction potential of the **[Co(triphos)(bdt)(H)]$^{0/-}$** (**IV-H/V**) couple is −1.61 V (see ESI† for details), and this value is well beyond our operating potential of −2.15 V. CVs at high scan rates do not display this trace-crossing behavior, indicating that the slow kinetics or the diffusion of **IV-H** can be outcompeted by the electron transfer step under these conditions (Fig. S20†). Additionally, all the CPE traces performed in the presence of proton donors (TFE or H_2O) indicate a slight increase in the current response in the first few minutes of starting the electrolysis, followed by a stabilization of the current (Fig. S27, S29, S30, S32, S34 and S35†), further supporting the hypothesis that a new species is generated in the diffusion layer upon starting the electrolysis. Intermediate **V** is proposed to react with CO_2 and lead to the formation of the formato-complex **VI** (Fig. S48†), followed by deligation of formate and religation of the apical phospine linker to regenerate **II** in a stepwise or concerted manner. Intermediate **V** can also directly reduce exogenous proton donors in solution to form H_2 as is observed in the electrolysis experiments.

Conclusions

This report focuses on the investigation of the electrocatalytic activity of **[Co(triphos)(bdt)]$^+$** towards the CO_2RR. In the presence of an exogenous proton source such as H_2O, selective electrochemical conversion of CO_2 to $HCOO^-$ is observed with faradaic yields as high as 94% at an overpotential of 750 mV. The catalyst displays robust stability, with 8 and 24 hours CPE experiments displaying negligible reduction in current and no evidence of degradation *via* deposition on the electrode during electrolysis. Chemical reduction studies of **[Co(triphos)(bdt)]$^+$** indicate that deligation of the apical phosphine likely occurs before catalysis. A mechanism is proposed to occur through a hydride transfer pathway, and DFT calculation indicate an additional reduction of the **[Co(triphos)(bdt)(H)]^0** to **[Co(triphos)(bdt)(H)]$^-$** is necessary for turnover, suggesting an overall ECEC mechanism. Ultimately, this study provides additional experimental evidence towards the beneficial role sulfur-based moieties play in molecular metal complexes as a method to increase their selectivity as electrocatalysts towards CO_2RR. Further studies are underway to improve aspects of this catalyst, such as the relatively large overpotential, through functionalization of the ancillary ligands.

Data availability

All the data supporting this article have been included in the main text and ESI.†

Author contributions

S. C. M. managed and directed the overall project and supervised the experimental work. J. A. I. also co-supervised the experimental work and performed initial electrochemical studies, NMR, and DFT calculations. D. A. V. performed additional electrochemical and mechanistic studies. J. A. I wrote this manuscript and D. A. V. co-wrote the manuscript with input from S. C. M. S. C. M, J. A. I., and D. A. V. reviewed and analyzed all data. S. F., E. M., and C. Y. assisted in experimental work and analyzed data. All the authors discussed the results and commented on the manuscript.

Conflicts of interest

There are no conflicts to declare.

Acknowledgements

The research was supported by the U. S. Department of Energy, Office of Basic Energy Sciences, Division of Chemical Sciences, Geosciences and Biosciences under Award DE-SC0019236. XPS data was collected at the Core Center of Excellence in Nano Imaging, USC. We would like to thank the National Science Foundation (award: CHE-2018740) for the purchase of the X-ray diffractometer used to solve the crystal structure reported here. Density functional theory calculations were performed with computational resources offered by the USC Center for Advanced Research Computing. We would like to thank Bianca Costa, Prof. Adam Smith, and his research group for permitting our use of their ion chromatograph for formate and oxalate detection and quantification.

References

1 IEA, *2018 World Energy Outlook: Executive Summary*, OECD/IEA, 2018, p. 35.
2 D. G. Nocera, *Acc. Chem. Res.*, 2017, **50**, 616–619.
3 R. J. Detz, J. N. H. Reek and B. C. C. Van Der Zwaan, *Energy Environ. Sci.*, 2018, **11**, 1653–1669.
4 R. L. House, N. Y. M. Iha, R. L. Coppo, L. Alibabaei, B. D. Sherman, P. Kang, M. K. Brennaman, P. G. Hoertz and T. J. Meyer, *J. Photochem. Photobiol., C*, 2015, **25**, 32–45.
5 Z. W. Seh, J. Kibsgaard, C. F. Dickens, I. Chorkendorff, J. K. Nørskov and T. F. Jaramillo, *Science*, 2017, **355**(6321), DOI: 10.1126/science.aad4998.
6 P. De Luna, C. Hahn, D. Higgins, S. A. Jaffer, T. F. Jaramillo and E. H. Sargent, *Science*, 2019, **364**(6438), eaav3506.

7 R. Francke, B. Schille and M. Roemelt, *Chem. Rev.*, 2018, **118**, 4631–4701.
8 A. Tatin, J. Bonin and M. Robert, *ACS Energy Lett.*, 2016, **1**, 1062–1064.
9 J. Cen, Q. Wu, M. Liu and A. Orlov, *Green Energy Environ.*, 2017, **2**, 100–111.
10 D. Kim, K. K. Sakimoto, D. Hong and P. Yang, *Angew. Chem., Int. Ed.*, 2015, **54**, 3259–3266.
11 A. M. Appel, J. E. Bercaw, A. B. Bocarsly, H. Dobbek, D. L. Dubois, M. Dupuis, J. G. Ferry, E. Fujita, R. Hille, P. J. A. Kenis, C. A. Kerfeld, R. H. Morris, C. H. F. Peden, A. R. Portis, S. W. Ragsdale, T. B. Rauchfuss, J. N. H. Reek, L. C. Seefeldt, R. K. Thauer and G. L. Waldrop, *Chem. Rev.*, 2013, **113**, 6621–6658.
12 D. T. Whipple and P. J. A. Kenis, *J. Phys. Chem. Lett.*, 2010, **1**, 3451–3458.
13 Y. Jiao, Y. Zheng, M. Jaroniec and S. Z. Qiao, *Chem. Soc. Rev.*, 2015, **44**, 2060–2086.
14 J. D. Benck, T. R. Hellstern, J. Kibsgaard, P. Chakthranont and T. F. Jaramillo, *ACS Catal.*, 2014, **4**, 3957–3971.
15 H. A. Gasteiger and N. M. Marković, *Science*, 2009, **324**, 48–49.
16 C. Rice, S. Ha, R. I. Masel, P. Waszczuk, A. Wieckowski and T. Barnard, *J. Power Sources*, 2002, **111**, 83–89.
17 N. D. Loewen, T. V. Neelakantan and L. A. Berben, *Acc. Chem. Res.*, 2017, **50**, 2362–2370.
18 R. Williams, R. S. Crandall and A. Bloom, *Appl. Phys. Lett.*, 1978, **33**, 381–383.
19 T. C. Johnson, D. J. Morris and M. Wills, *Chem. Soc. Rev.*, 2010, **39**, 81–88.
20 W. H. Wang, Y. Himeda, J. T. Muckerman, G. F. Manbeck and E. Fujita, *Chem. Rev.*, 2015, **115**, 12936–12973.
21 S. Amanullah, P. Saha, A. Nayek, M. E. Ahmed and A. Dey, *Chem. Soc. Rev.*, 2021, **50**, 3755–3823.
22 C. R. Carr and L. A. Berben, in *CO_2 Hydrogenation Catalysis*, 2021, pp. 237–258.
23 P. Kang, T. J. Meyer and M. Brookhart, *Chem. Sci.*, 2013, **4**, 3497–3502.
24 S. T. Ahn, E. A. Bielinski, E. M. Lane, Y. Chen, W. H. Bernskoetter, N. Hazari and G. T. R. Palmore, *Chem. Commun.*, 2015, **51**, 5947–5950.
25 P. Kang, C. Cheng, Z. Chen, C. K. Schauer, T. J. Meyer and M. Brookhart, *J. Am. Chem. Soc.*, 2012, **134**, 5500–5503.
26 B. M. Ceballos and J. Y. Yang, *Proc. Natl. Acad. Sci. U. S. A.*, 2018, **115**, 12686–12691.
27 B. M. Ceballos and J. Y. Yang, *Organometallics*, 2020, **39**, 1491–1496.
28 D. W. Cunningham, J. M. Barlow, R. S. Velazquez and J. Y. Yang, *Angew. Chem., Int. Ed.*, 2020, **59**, 4443–4447.
29 D. W. Cunningham and J. Y. Yang, *Chem. Commun.*, 2020, **56**, 12965–12968.
30 H. D. Manamperi, C. E. Moore and C. Turro, *Chem. Commun.*, 2021, **57**, 1635–1638.
31 A. Taheri, E. J. Thompson, J. C. Fettinger and L. A. Berben, *ACS Catal.*, 2015, **5**, 7140–7151.
32 A. Taheri and L. A. Berben, *Inorg. Chem.*, 2016, **55**, 378–385.
33 S. Roy, B. Sharma, J. Pécaut, P. Simon, M. Fontecave, P. D. Tran, E. Derat and V. Artero, *J. Am. Chem. Soc.*, 2017, **139**, 3685–3696.
34 M. H. Rønne, D. Cho, M. R. Madsen, J. B. Jakobsen, S. Eom, É. Escoudé, H. C. D. Hammershøj, D. U. Nielsen, S. U. Pedersen, M.-H. Baik, T. Skrydstrup and K. Daasbjerg, *J. Am. Chem. Soc.*, 2020, **142**, 4265–4275.
35 S. Dey, F. Masero, E. Brack, M. Fontecave and V. Mougel, *Nature*, 2022, **607**, 499–506.
36 J. Bi, P. Hou, F. W. Liu and P. Kang, *ChemSusChem*, 2019, **12**, 2195–2201.
37 J. C. Fontecilla-Camps, P. Amara, C. Cavazza, Y. Nicolet and A. Volbeda, *Nature*, 2009, **460**, 814–822.
38 V. Svetlitchnyi, C. Peschel, G. Acker and O. Meyer, *J. Bacteriol.*, 2001, **183**, 5134–5144.
39 H. Dobbek, *Coord. Chem. Rev.*, 2011, **255**, 1104–1116.
40 T. Reda, C. M. Plugge, N. J. Abram and J. Hirst, *Proc. Natl. Acad. Sci. U. S. A.*, 2008, **105**, 10654–10658.
41 M. Guiral-Brugna, M. T. Giudici-Orticoni, M. Bruschi and P. Bianco, *J. Electroanal. Chem.*, 2001, **510**, 136–143.
42 F. A. Armstrong and J. Hirst, *Proc. Natl. Acad. Sci. U. S. A.*, 2011, **108**, 14049–14051.
43 S. Dey, M. E. Ahmed and A. Dey, *Inorg. Chem.*, 2018, **57**, 5939–5947.
44 M. E. Ahmed, A. Rana, R. Saha, S. Dey and A. Dey, *Inorg. Chem.*, 2020, **59**, 5292–5302.
45 S. Dey, T. K. Todorova, M. Fontecave and V. Mougel, *Angew. Chem., Int. Ed.*, 2020, **59**, 15726–15733.
46 N. M. Orchanian, L. E. Hong, D. A. Velazquez and S. C. Marinescu, *Dalton Trans.*, 2021, **50**, 10779–10788.
47 T. Fogeron, T. K. Todorova, J. P. Porcher, M. Gomez-Mingot, L. M. Chamoreau, C. Mellot-Draznieks, Y. Li and M. Fontecave, *ACS Catal.*, 2018, **8**, 2030–2038.
48 T. Fogeron, P. Retailleau, M. Gomez-Mingot, Y. Li and M. Fontecave, *Organometallics*, 2019, **38**, 1344–1350.
49 A. Mouchfiq, T. K. Todorova, S. Dey, M. Fontecave and V. Mougel, *Chem. Sci.*, 2020, **11**, 5503–5510.
50 F. Wang, A. T. Cannon, M. Bhattacharya, R. Baumgarten, R. T. VanderLinden and C. T. Saouma, *Chem. Commun.*, 2020, **56**, 12142–12145.
51 S. C. Marinescu, J. R. Winkler and H. B. Gray, *Proc. Natl. Acad. Sci. U. S. A.*, 2012, **109**, 15127–15131.
52 J. Schneidewind, R. Adam, W. Baumann, R. Jackstell and M. Beller, *Angew. Chem., Int. Ed.*, 2017, **56**, 1890–1893.
53 C. P. Yap, K. Hou, A. A. Bengali and W. Y. Fan, *Inorg. Chem.*, 2017, **56**, 10926–10931.
54 C. A. Ghilardi, F. Laschi, S. Midollini, A. Orlandini, G. Scapacci and P. Zanello, *J. Chem. Soc., Dalton Trans.*, 1995, **1**, 531.
55 S. Vogel, G. Huttner and L. Zsolnai, *Z. Naturforsch., B: J. Chem. Sci.*, 1993, **48**, 641–652.
56 J. A. Intrator, N. M. Orchanian, A. J. Clough, R. Haiges and S. C. Marinescu, *Dalton Trans.*, 2022, **51**, 5660–5672.
57 V. Körner, A. Asam, G. Hüttner, L. Zsolnai and M. Büchner, *Z. Naturforsch., B: J. Chem. Sci.*, 1994, **49**, 1183–1192.
58 X. Su, K. M. McCardle, L. Chen, J. A. Panetier and J. W. Jurss, *ACS Catal.*, 2019, **9**, 7398–7408.

59 D. A. Gangi and R. R. Durand, *J. Chem. Soc. Chem. Commun.*, 1986, **9**, 697–699.
60 M. H. Schmidt, G. M. Miskelly and N. S. Lewis, *J. Am. Chem. Soc.*, 1990, **112**, 3420–3426.
61 T. F. Connors, J. V. Arena and J. F. Rusling, *J. Phys. Chem.*, 1988, **92**, 2810–2816.
62 C. Amatore, J. Pinson, J. M. Savéant and A. Thiebault, *J. Electroanal. Chem. Interfacial Electrochem.*, 1980, **107**, 59–74.
63 E. Portenkirchner, K. Oppelt, C. Ulbricht, D. A. M. Egbe, H. Neugebauer, G. Knör and N. S. Sariciftci, *J. Organomet. Chem.*, 2012, **716**, 19–25.
64 C. Costentin, S. Drouet, M. Robert and J.-M. Savéant, *Science*, 2012, **338**, 90–94.
65 B. H. Solis and S. Hammes-Schiffer, *J. Am. Chem. Soc.*, 2012, **134**, 15253–15256.
66 K. Chen, C. A. Downes, E. Schneider, J. D. Goodpaster and S. C. Marinescu, *ACS Appl. Mater. Interfaces*, 2021, **13**, 16384–16395.
67 K. M. Waldie, A. L. Ostericher, M. H. Reineke, A. F. Sasayama and C. P. Kubiak, *ACS Catal.*, 2018, **8**, 1313–1324.